



Photocatalytic degradation of fluoroquinolone antibiotics using ordered mesoporous $\text{g-C}_3\text{N}_4$ under simulated sunlight irradiation: Kinetics, mechanism, and antibacterial activity elimination



Fengliang Wang^a, Yiping Feng^a, Ping Chen^b, Yingfei Wang^a, Yuehan Su^a, Qianxin Zhang^a, Yongqin Zeng^a, Zhijie Xie^a, Haijin Liu^c, Yang Liu^d, Wenyng Lv^a, Guoguang Liu^{a,*}

^a Institute of Environmental Health and Pollution Control, School of Environmental Science and Engineering, Guangdong University of Technology, Guangzhou, Guangdong 510006, China

^b School of Environment, Tsinghua University, Beijing, 100084, China

^c School of Environment, Henan Normal University, Key Laboratory for Yellow River and Huaihe River Water Environment and Pollution Control, Xinxiang, 453007, China

^d Guangdong University of Petrochemical Technology, Maoming, 525000, China

ARTICLE INFO

Keywords:
Fluoroquinolones
 $\text{ompg-C}_3\text{N}_4$
Kinetics
Mechanism
Antibacterial activity

ABSTRACT

The occurrence of fluoroquinolones (FQs) in the ambient environment has raised serious concerns. In this study, the photocatalytic degradation kinetics and mechanism of ciprofloxacin (CIP) was investigated in ordered mesoporous $\text{g-C}_3\text{N}_4$ ($\text{ompg-C}_3\text{N}_4$). Under simulated sunlight irradiation, $\text{ompg-C}_3\text{N}_4$ exhibited a 2.9 fold more rapid reaction for CIP degradation than bulk $\text{g-C}_3\text{N}_4$. This enhancement may be attributed to the large specific surface area and effective charge separation of $\text{ompg-C}_3\text{N}_4$. The eradication of CIP followed the Langmuir–Hinshelwood (L–H) kinetics model, and surface reactions played a significant role during the photocatalysis process. Further study of reactive species (RSs) by both ESR technology and RSs scavenging experiments revealed that the superoxide anion radical ($\text{O}_2^{\cdot -}$) and photohole (h^+) were primarily responsible for the degradation of CIP. Based on the identification of intermediates using liquid chromatography with tandem mass spectrometry (HPLC-MS/MS), and the prediction of reactive sites via Frontier Electron Densities (FEDs), the degradation pathways of CIP were proposed. A comparison of the degradation among FQs revealed that the piperazine moiety showed a dramatic effect on the degradation of FQs during the photocatalysis process. A residual antibiotic activity experiment revealed that $\text{ompg-C}_3\text{N}_4$ provided a very desirable performance for the reduction of antibiotic activity. The sufficient photocatalytic degradation of CIP in ambient water revealed that a sunlight-driven $\text{ompg-C}_3\text{N}_4$ photocatalytic process may be efficiently applied for the remediation of CIP contaminated natural waters.

1. Introduction

In recent years, the presence of antibiotics in wastewater and drinking water has attracted increasing concern [1,2]. Fluoroquinolones antibiotics (FQs) are one type of the most important synthetic antibiotics that are widely employed to treat infections caused by a broad spectrum of bacterial species [3,4]. Due to their stable chemical structures and recalcitrance to biological degradation, most of FQs cannot be effectively removed by conventional sewage treatment processes [5]. Therefore, FQs have been frequently detected with noticeable concentrations (e.g., from 0.6 to 5.6 $\mu\text{g/L}$) in aqueous environments [6,7]. It has been demonstrated that antibiotic residues in the environment could result in the evolution of novel antibiotic resistant

bacteria that ultimately pose threat to the public health [8,9]. Thus, new techniques for the treatment of water resident FQs are required.

Currently, advanced oxidation processes (AOPs) have been developed to remove FQs from wastewater [9–11]. Photocatalytic technology, as a type of AOPs, has received intensive attention due to its high efficiency and enduring stability [12]. Many traditional photocatalysts (e.g., TiO_2), have exhibited the capacity to degrade these FQs through the generation of reactive oxygen species (ROS) under UV light irradiation [13]. However, the poor light harvesting ability, narrow applicable range of pH, difficult separation, potential ecotoxicity of these photocatalysts hindered their practical application [14,15], and therefore, the development of environment friendly and highly pH tolerant sunlight/light-driven photocatalysts is required.

* Corresponding author.
E-mail address: liugg615@163.com (G. Liu).

Due to the unique photoelectric properties, non-toxic, and environment friendly with biocompatibility graphitic carbon nitride ($\text{g-C}_3\text{N}_4$) has garnered intensive attention as a photocatalyst, and has shown great potential applications in hydrogen production [16], CO_2 reduction [17], and pollutant degradation [18]. However, the low specific surface area ($< 10 \text{ m}^2/\text{g}$), as well as high recombination rates of photogenerated electron-hole pairs of bulk $\text{g-C}_3\text{N}_4$ largely reduced its photocatalytic performance, which greatly limits its practical applications [19]. In order to address these limitations, several techniques including nanostructure fabrication [20], metal or non-metal doping [21], and semiconductor coupling [22] have been employed. The fabrication of porous $\text{g-C}_3\text{N}_4$ has been considered to be the most effective way to enhance its photocatalytic activity [20]. The high specific surface area of porous $\text{g-C}_3\text{N}_4$ can increase the population of available active sites and thus enhances its absorption capacity. In addition, because of the short diffusion path of electrons from the interior to the surface, the recombination rates of photogenerated electron-hole pairs of porous $\text{g-C}_3\text{N}_4$ may be largely restrained [23]. Previous studies have described the synthesis of ordered mesoporous $\text{g-C}_3\text{N}_4$ (ompg- C_3N_4), which exhibited excellent photocatalytic performance in the degradation of dyes [23].

To date, various $\text{g-C}_3\text{N}_4$ based materials, including $\text{g-C}_3\text{N}_4$ [24], graphitic $\text{C}_3\text{N}_4/\text{Ag}_3\text{PO}_4$ [25], Au-porous graphitic $\text{C}_3\text{N}_4/\text{graphene}$ [26], and graphene quantum dots- BiVO_4 /graphitic C_3N_4 [27], have also been developed for the degradation of FQs. These studies mainly reported on the synthesis procedures of the photocatalysts, as well as revealing their degradation efficiencies toward FQs. Nevertheless, the photocatalytic degradation kinetics of FQs by these $\text{g-C}_3\text{N}_4$ based photocatalysts have not yet been reported. Moreover, relationships between the chemical reactivity and molecular structures of FQs during the $\text{g-C}_3\text{N}_4$ based photocatalytic process remain unknown. Furthermore, data relating to the residual antibacterial activity of treated FQ solutions during the $\text{g-C}_3\text{N}_4$ based photocatalytic process has not been obtained. Therefore, further studies are required to elucidate the degradation mechanisms of FQs via $\text{g-C}_3\text{N}_4$ based photocatalysts.

In this study, a sunlight-driven photocatalyst (ompg- C_3N_4) was synthesized, employing SBA-15 as a hard template. The photocatalytic degradation kinetics and mechanism of a recalcitrant FQs, Ciprofloxacin (CIP) under simulated sunlight irradiation was investigated. The degradation pathways of the CIP were deduced based on product identification by HPLC-MS/MS, as well as reactive sites prediction. The degradation of CIP was compared with other FQs in order to understand the relationship between the degradation reactivity and molecular structures of FQs. The reduction of antibacterial activity during the photocatalytic process was assessed through an *E. coli* inhibition zone test. Finally, the effects of specific water constituents and various water matrices on the photocatalytic degradation of FQs were investigated.

2. Method

2.1. Materials

Ciprofloxacin (CIP, 98%), norfloxacin (NOR, 98%), enrofloxacin (ENR, 98%), norfloxacin (NOR, 98%), ofloxacin (OFL, 98%), lomefloxacin (LOM, 98%), fleroxacin (FLE, 98%), and flumequine (FLU, 98%), tetraethyl orthosilicate, and dicyandiamide were purchased from Aladdin (America). Poly (ethylene glycol)-block-poly (propylene glycol)-block-poly copolymer Pluronic P123 (EO20PO70EO20, Mn = 5800) was obtained from Aldrich (America). HPLC-grade acetonitrile and methanol were obtained from CNW Technologies GmbH (Germany). Other reagents were at least of analytical grade and used as received without further purification. Deionized (DI) water was prepared by a Milli-Q apparatus (Germany). River water was collected from Zhujiang, Guangzhou. Secondary wastewater effluent was collected from local wastewater treatment plants (WWTP) in Guangzhou,

China. Seawater was obtained from the South China Sea in Huizhou, Guangdong province. All water samples were filtered by 0.45 μm fiber membrane and preserved in the dark at 4 °C. The primary properties of the water samples were listed in Table S1.

2.2. Preparation and characterization of photocatalysts

The SBA-15 was synthesized according to a previous report, with a slight improvement. The ompg- C_3N_4 was prepared by utilizing SBA-15 as the template [28]. Bulk $\text{g-C}_3\text{N}_4$ was synthesized by the direct thermal polycondensation of dicyandiamide [21]. Details on the preparation of the photocatalysts are provided in Text S1.

A transmission electron microscope (TEM, JEM-2100HR) was employed to observe the microscopic morphology of the samples. The crystal structure was examined by X-ray diffraction (XRD, BRUKER D8 ADVANCE) with Cu K α radiation ($\lambda = 0.154178 \text{ nm}$). The surface areas and pore sizes of the as-prepared samples were analyzed by the nitrogen adsorption-desorption isotherms (BET, BECKMAN COULTER SA3100). Light absorption properties were detected via a UV-vis spectrophotometer (Shimadzu UV 2450) using BaSO_4 powder as the reflectance standard. Photoluminescence spectra were recorded with a FluoroMax-4 fluorescence spectrophotometer (HORIBA Jobin Yvon).

2.3. Photocatalytic degradation of FQs

The photocatalytic degradation of CIP and other fluoroquinolones were carried out in a XPA-7 rotary photochemical reactor (Fig. S1, Nanjing Xujiang Electromechanical plant). The simulated sunlight source was provided by a 350 W xenon lamp with a 290 nm cut-off filter. For each experiment, 50 mL of a 4 mg/L FQs aqueous solution that contained 1.0 g/L catalysts were introduced into a quartz tube. The pH of the reaction solution was adjusted by adding a 0.1% NaOH or H_2SO_4 solution. Prior to irradiation, the reaction solution was magnetically stirred in the dark for 30 min in order to obtain an adsorption-desorption equilibrium of FQs on the photocatalyst. During irradiation, aliquots of samples (1.0 mL) were withdrawn at predetermined time intervals and filtered through 0.22 μm Millipore filters to remove the photocatalyst. The residual FQs in the solution were analyzed through high performance liquid chromatography (HPLC).

2.4. Determination of RSs

An electron spin resonance (ESR) technique was carried out to directly detect the RSs. The ESR signals of hydroxyl radicals ($\cdot\text{OH}$) and superoxide anion radicals ($\text{O}_2^{\cdot -}$) trapped by 5,5-dimethyl-1-pyrroline N-oxide (DMPO) were recorded under ambient temperatures with a Bruker JES-FA200 spectrometer. ESR signals of ${}^1\text{O}_2$ trapped by 4-oxo-2,2,6,6-tetramethylpiperidine were analyzed by a Bruker A200e 9.5/12. Detailed analytical conditions may be found in Text S2.

Radical scavenging experiments were also conducted for the indirect analysis of the RSs during the photodegradation process. 1.0 mM benzoquinone (BQ), 10 mM isopropanol (IPA), 10 mM $\text{Na}_2\text{C}_2\text{O}_4$, 75 mM sodium azide (NaN_3), and 50 μM $\text{K}_2\text{Cr}_2\text{O}_7$ were added into the reaction solution as the scavengers of superoxide iron radical ($\text{O}_2^{\cdot -}$), hydroxyl radical ($\cdot\text{OH}$), photogenerated hole (h^+), singlet oxygen (${}^1\text{O}_2$), and photogenerated electron (e^-), respectively [28–30].

2.5. Analysis

Residual FQs in solution were analyzed by LC-20A high performance liquid chromatography (HPLC) (Shimadzu, Japan). The detailed analytical method may be found in Text S3 and Table S2.

To detect the degradation products of CIP, a C18 solid phase extraction (SPE) cartridge (6 cc/200 mg, WAT106202) was applied to concentrate the reaction products. The byproducts of CIP were then analyzed with an Agilent 1100 series HPLC coupled to a 6410 triple

quadrupole mass spectrometer (Agilent Technologies, USA). The detail analytical method is listed in Text S4.

To evaluate the mineralization efficiency, the total organic carbon (TOC) of the reaction solutions was measured via a TOC analyzer (TOC-V CPH E200V, Shimadzu Co., Japan).

A Metrohm ion chromatograph (IC) 883 was used to analyze the anions, with the separation being performed in an ion chromatography column (Assup-5, 250/4.0 mm). An isocratic elution consisting of 3.2 mM Na₂CO₃/1.0 mM NaHCO₃ at flow rate of 1 mL/min was employed as the mobile phase.

2.6. Theoretical calculation

Molecular orbital calculations and stationary point geometries were derived through a hybrid density functional B3LYP method with the 6-311G+ (d, p) basis set (B3LYP/6-311G+ (d, p)). Fig. S2 presents the optimized structure and atomic numbering of the CIP. The frontier electron densities (FEDs) of the highest occupied molecular orbital (HOMO) and the lowest unoccupied molecular orbital (LUMO) were calculated. Values of 2 FED_{HOMO}, FED_{HOMO} + FED_{LUMO}, and point charge were calculated to predict the reaction sites for h⁺, ·OH, and O₂^{·-} attacks [31,32].

2.7. Residual antibiotic activity test

The residual antibiotic activity was determined by measuring the inhibition halo that was formed around the sensi-discs on an agar plate. Initially, the agar plates were respectively inoculated with 1.2 × 10⁸ CFU/mL E.coli, and parallel 10 µL reaction samples were separately spiked on agar plates. Following 24 h of incubation at 37 °C, the growth inhibition halo diameter around the sensi-discs was measured.

3. Results and discussion

3.1. Characterization of ompg-C₃N₄

The morphology of the ompg-C₃N₄ was investigated using TEM. Fig. 1a and b revealed a 1D straight channeling structure with a pore size of ca. 5.6 nm. The adsorption/desorption isotherms and pore size distributions in Fig. 1c demonstrated that ompg-C₃N₄ exhibited a bi-modal mesoporous structure with a pore size of ca. 5.6 nm, which was coincided well with the results obtained by the TEM. In addition, the specific surface area of ompg-C₃N₄ (50.1 m²/g) was far higher than that of bulk g-C₃N₄ (16.7 m²/g). The XRD spectrum in Fig. S3 shows that both the bulk g-C₃N₄ and ompg-C₃N₄ exhibited two distinct diffraction peaks, at 2θ = 27.5° and 13.0°, which may be indexed to the interlayer stacking structure of aromatic segments (002) and the in-plane structural packing motif of tri-s-triazine units (100) (JCPDS Card No. 87-1526). UV-vis DRS of ompg-C₃N₄ displayed in Fig. S4 shows that ompg-C₃N₄ exhibited high photo-absorption capacity for visible light, which suggested the potential photocatalytic activity of ompg-C₃N₄ under simulated sunlight. A photoluminescence (PL) spectrum was subsequently performed to investigate the recombination rate of electron-holes, as shown in Fig. 1(d). Clearly, the PL emission spectrum of bulk g-C₃N₄ revealed a strong emission peak at ~463 nm when excited at a wavelength of 380 nm, while obvious fluorescence quenching was observed for ompg-C₃N₄, indicating that the mesoporous structure might highly improve the electron transfer capability of ompg-C₃N₄. In summary, mesoporous structured of ompg-C₃N₄ can provide additional active sites and higher electron transfer capacities, which serve to enhance the photocatalytic activities of ompg-C₃N₄.

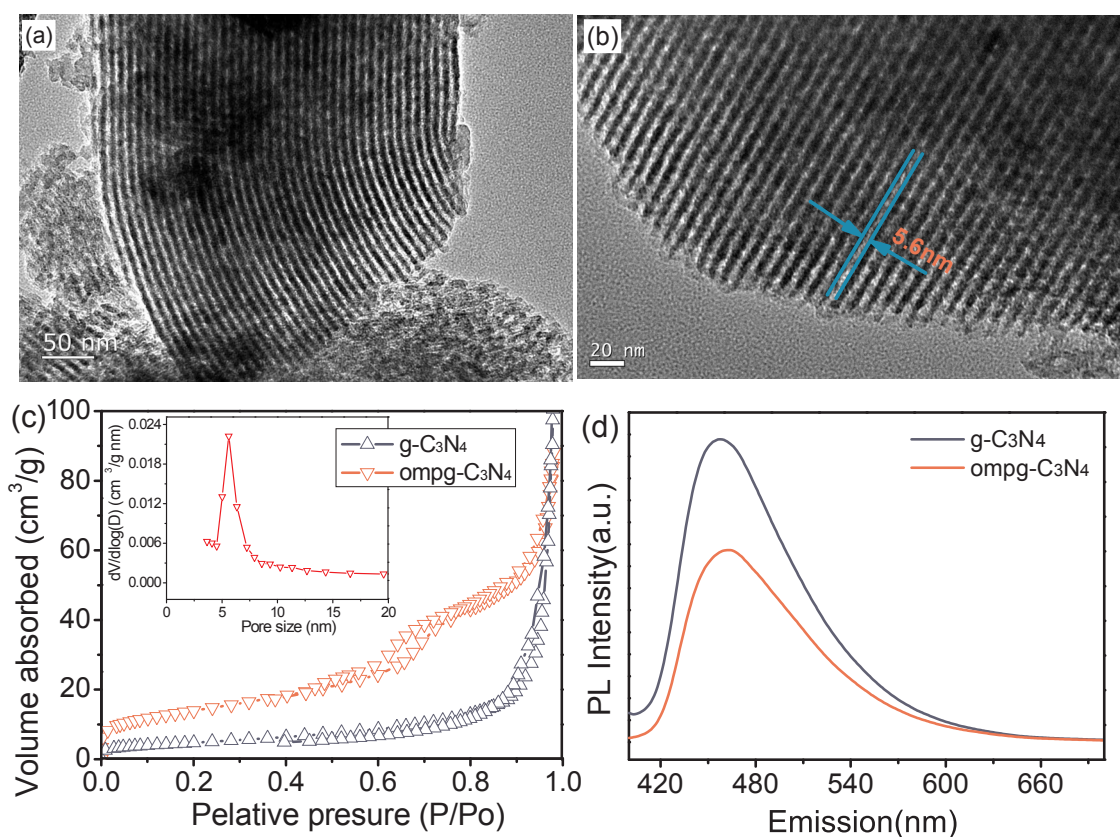


Fig. 1. (a) and (b) TEM images of ompg-C₃N₄; (c) The N₂ adsorption–desorption isotherms of ompg-C₃N₄. (Inset: Pore size distributions of ompg-C₃N₄); (d) PL spectra of ompg-C₃N₄ under 380 nm excitation.

3.2. Photocatalytic degradation kinetics of CIP

3.2.1. Effect of catalyst dosage

Fig. 2(a) reveals that the concentration of CIP was not altered in the absence of photocatalyst, which verified the photochemical stability of CIP under simulated sunlight irradiation. The adsorption experiment showed that 24.1% CIP was absorbed by ompg- C_3N_4 under dark conditions. In contrast, bulk $\text{g-C}_3\text{N}_4$ exhibited a degradation efficiency of 61.2% in 50 min by simulated sunlight irradiation. Significantly, a significant enhancement in the degradation of CIP was obtained by ompg- C_3N_4 , e.g., 92.3% of CIP can be decomposed with ompg- C_3N_4 over the same timeline, which was ~ 2.9 times higher than that by the bulk $\text{g-C}_3\text{N}_4$.

Fig. 2(b) illustrates the effect of the $\text{ompg-C}_3\text{N}_4$ concentration on the photocatalytic degradation of CIP. As the loading amount of the $\text{ompg-C}_3\text{N}_4$ was increased from 0.2 to 1.0 g/L, the pseudo-first-order rate constants (k_{obs}) of CIP increased from 0.0266 to 0.0438 min⁻¹. However, further increases in catalyst loading led to an evident decrease of degradation efficiency due to the excess catalyst acts as scatter or reflects photons to hinder the excitation of the photocatalyst. Moreover, with increasing quantities of photocatalyst, the population of active sites was found to be reduced due to the aggregation of photocatalyst particles [33].

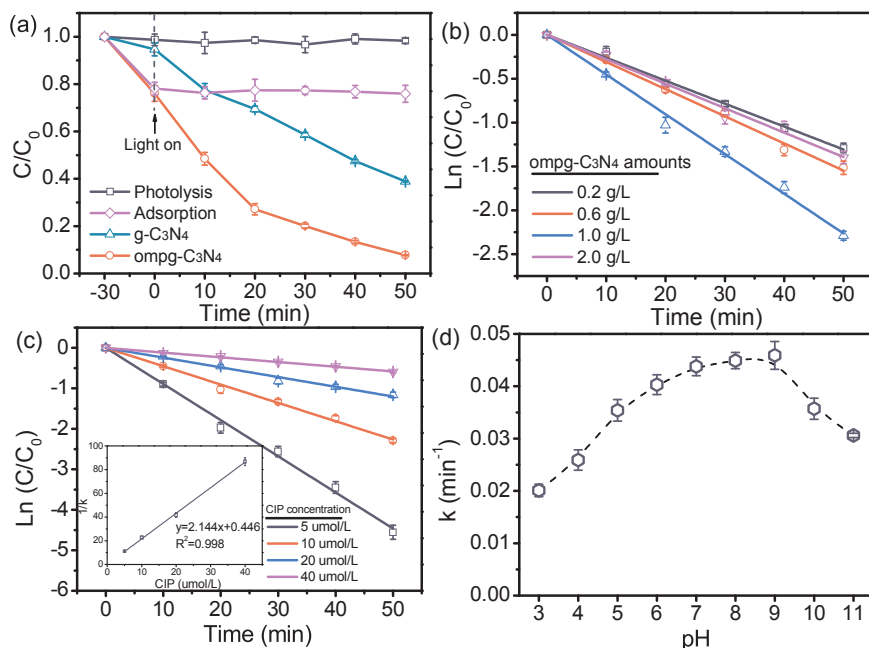
3.2.2. Effect of initial CIP concentration

Fig. 2(c) presents the effects of different initial concentrations of CIP by a simulated sunlight ompg-C₃N₄ process. It was observed that an increase of initial substrate concentrations, from 5.0 to 40.0 μmol/L, led to the rate constants of CIP decreased from 0.0887 to 0.0115 min⁻¹. One possible reason might be that higher concentrations of CIP absorbed the incident light reduced the photons to activate ompg-C₃N₄, resulting in the low degradation rate of CIP [34].

Further, the Langmuir–Hinshelwood (LH) model was used to confirm whether the solid–liquid interface was the site that dominated the heterogeneous photocatalytic degradation [35]. The L–H model was described as follow:

$$\frac{1}{k} = \frac{[CIP]_0}{k_{I,H}} + \frac{1}{k_{I,H} k_I} \quad (1)$$

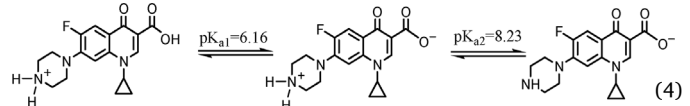
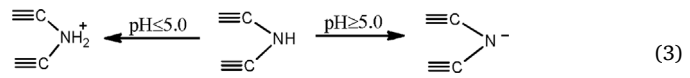
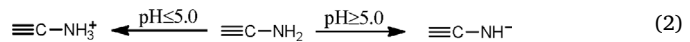
where k was the pseudo-first-order rate constant (min^{-1}), $[\text{CIP}]_0$ was the initial concentration of CIP ($\mu\text{mol/L}$), k_{LH} presents the L-H



adsorption constant of CIP over ompg-C₃N₄ surface (μmol^{-1}), and k_L is the intrinsic reaction rate constant ($\mu\text{mol}/\text{min}$). It may be observed in the inset of Fig. 2(c) that the photocatalytic degradation of CIP aligned well with the L-H kinetic model ($R^2 = 0.998$), indicating that the degradation of CIP primarily occurred on the surface of the ompg-C₃N₄. The adsorption constant k_{LH} was calculated as $0.467 \mu\text{M}^{-1}$, and the intrinsic reaction rate constant K_L was obtained as $4.803 \mu\text{M}/\text{min}$.

3.2.3. Effect of pH

The influence of pH on the ompC_3N_4 mediated photocatalytic degradation of CIP was evaluated, as shown in Fig. 2(d). It was found that an increase of pH, from 3.0 to 9.0 resulted in the increase of the rate constants, of CIP from 0.0201 to 0.0459 min^{-1} . However, a further increase in pH, from 9.0 to 11.0, led to a decrease in the degradation efficiency. Since the isoelectric point of ompC_3N_4 was ca. 5.0 and the pKa of CIP was reported to be 6.16 and 8.23 [36], the existing forms of ompC_3N_4 and CIP in different pH solutions could be described according the Eqs. (2)–(4).



It has been proposed that electrostatic repulsion between protonated CIP and the positively charged ompg-C₃N₄ may take place at pH < 5.0, which significantly inhibited the photocatalysis. Moreover, in a low pH (< 5.0), large amounts of H⁺ may be absorbed on the surface of ompg-C₃N₄ via N...H interactions, which compete with CIP for active sites (tri-s-triazine units) [19]. When the pH was above 5.0, electrostatic attraction occurred between protonated CIP and negatively charged ompg-C₃N₄, resulting in enhanced photocatalytic degradation. However, the repulsive force between CIP and ompg-C₃N₄ was intensified as further increase pH due to their deprotonation, and led to a lower CIP degradation efficiency. ompg-C₃N₄ exhibited a higher photocatalytic efficiency for CIP across a rather wide pH range (from pH 5.0 to 11.0) than commercial P25 and other common photocatalysts [31,37,38]. This superior property might be attributed to the π-π

Fig. 2. (a) Comparison of absorption, photolysis and photocatalysis of CIP under simulated sunlight irradiation; (b) effect of $\text{ompg-C}_3\text{N}_4$ dosage on the photocatalytic degradation kinetics of CIP; (c) effect of CIP initial concentration on the photocatalytic degradation kinetics of CIP. (Inset: The relationship between $1/K$ and the initial concentration of CIP); (d) Kinetic rate constants of CIP degradation under different pH values. Error bars represent the standard deviation of 2 replicates.

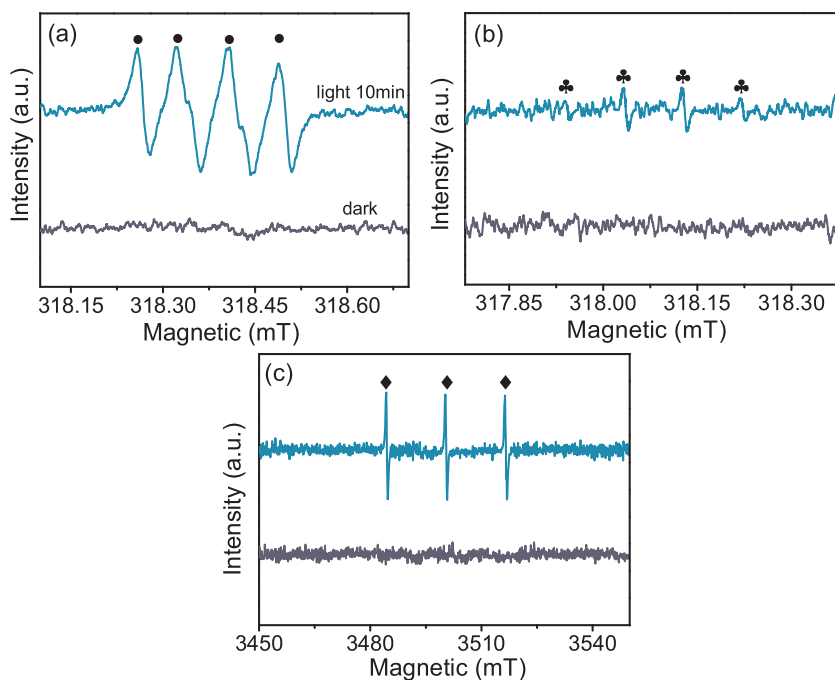


Fig. 3. ESR spectra of the (a) DMPO- O_2^- adducts, (b) DMPO-OH adducts, and (c) adduct of ${}^1\text{O}_2$ and TEMP, recorded under simulated sunlight irradiation. [DMPO] = 50 mM, [ompg-C₃N₄] = 1.0 g/L, [CIP] = 10 $\mu\text{mol}/\text{L}$.

interactions between aromatic organic compounds and ompg-C₃N₄ [19], indicating that ompg-C₃N₄ might be suitable for the treatment of industrial wastewater under variable pH values.

3.3. Preliminary photocatalytic mechanism of CIP

3.3.1. Roles of reactive species

Previous studies have hypothesized that various reactive species (RSs), such as O_2^- , $\cdot\text{OH}$, h^+ , and e^- were generated during the ompg-C₃N₄ photocatalytic process [21]. As depicted in Fig. 3, no ESR signal could be found under dark conditions. However, a strong four-line ESR characteristic signal for DMPO- O_2^- , and a weak signal for the DMPO- $\cdot\text{OH}$ spin adduct were observed under simulated sunlight irradiation, indicating the existence of O_2^- and $\cdot\text{OH}$. Moreover, the characteristic 1:1:1 triplet signal of the TEMP- ${}^1\text{O}_2$ adduct was the clear evidence of ${}^1\text{O}_2$ generation in the photocatalytic system.

In order to discriminate the contributions of different RSs to the photocatalytic degradation of CIP, radical trapping experiments were carried out through the addition of BQ, IPA, NaN₃, Na₂C₂O₄, and K₂Cr₂O₇. As shown in Table 1, with the addition of IPA and NaN₃, the degradation rates of CIP were slightly decreased, with inhibition rates of 9.8% and 15.2%, respectively. However, the BQ and Na₂C₂O₄ lead to significant inhibitory effects on the degradation of CIP, which were found to be 88.2% and 60.5% of the inhibition rate. These results indicated that O_2^- and photogenerated h^+ played critical roles in the photocatalytic degradation of CIP. Moreover, adding K₂Cr₂O₇ significantly inhibited the degradation of CIP, indicating that e^- also played a vital role in the photocatalytic process. It was proposed that

O_2^- may be generated from e^- by capturing oxygen in solution, suggesting that e^- might participate in the photocatalytic degradation of CIP by generating O_2^- [21].

3.3.2. Product identification

In order to investigate the structural photocatalytic mechanism of CIP, the photocatalytic transformation products (TPs) were identified by using a LC-MS/MS technique. The structural identification of these intermediates (P1-P11) is summarized in Table S3. TPs with m/z 362, 334, 306, 291, and 264 arose from the cleavage of the piperazine ring. TPs with m/z 330, 261, and 318 proved to be the defluorination products of CIP, whereas m/z 364 and 304 were derived from the cleavage of the quinolone ring and carboxyl group, and m/z 348 was identified as the hydroxylation product of CIP. Moreover, m/z 318 was proposed as the cyclopropane ring cleavage products of CIP. Among them, m/z 362, 334, 306, 291, 264, 330, 261, 318, and 304 have previously been detected in other oxidation processes, while m/z 348 has been found in the degradation of a simulated norfloxacin structure by persulfate [5,9,39,40].

3.3.3. Mineralization and the detection of inorganic ions

The decrease of total organic carbon (TOC) was measured to evaluate the extent of mineralization during the photocatalytic degradation of CIP (Fig. 4(a)). After 50 min of treatment, the loss of CIP attained 92.3%, while only 42.5% of TOC removal was observed, indicating that the intermediates toward the photocatalytic process are more stable than that of CIP. However, ca. 56.7% TOC was removed after 100 min of irradiation, implying that total mineralization could be achieved with longer irradiation times.

The inorganic ions generated from the degradation of CIP were determined by IC. As shown in Fig. 4(b), F⁻ and NO₃⁻ were gradually formed during the degradation of CIP. In addition, the defluorination and piperazine ring cleavage products of CIP have also been detected by LC-MS/MS, which indicated that the piperazine ring and fluorine of CIP were vulnerable to RSs attack and may be cleaved from molecular CIP during the photocatalytic process.

3.3.4. Reactive site identification

In order to well understand the primary reactive sites of the CIP molecule for RSs attack during the ompg-C₃N₄ photocatalysis, the

Table 1
Kinetic rate constant of CIP degradation with the addition of different scavengers.

Quencher	RSs Quenched	K _{obs} (min^{-1})	Inhibition rate/%
Control	–	0.0438	0
BQ	O_2^-	0.0052	88.2
Na ₂ C ₂ O ₄	h^+	0.0173	60.5
K ₂ Cr ₂ O ₇	e^-	0.0041	90.7
IPA	$\cdot\text{OH}$	0.0395	9.8
NaN ₃	${}^1\text{O}_2$	0.0371	15.2

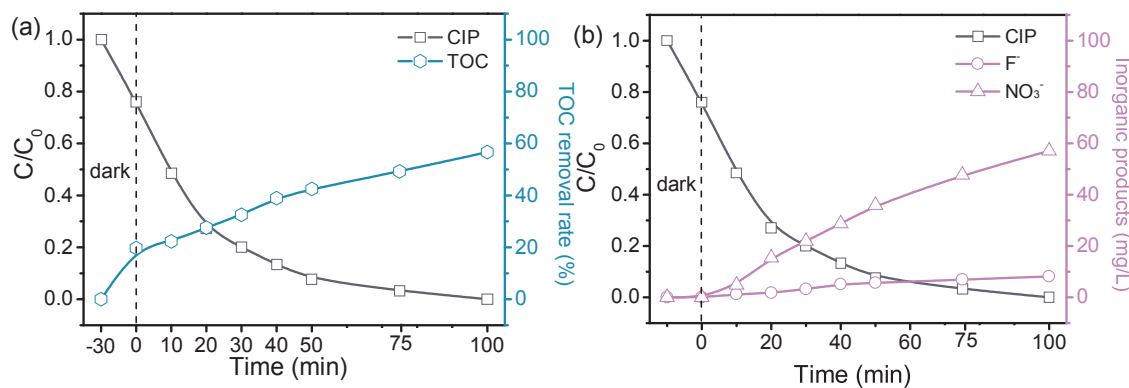


Fig. 4. Change of (a) TOC removal and (b) inorganic products concentration during the ompg-C₃N₄ photocatalytic degradation process.

frontier electron densities (FEDs) of CIP were calculated, as summarized in Table S4. According to Frontier Orbital Theory, positions with a more positive point charge were more easily attacked by O₂^{·-}, while h⁺ typically attacked the positions with higher values of 2FED_{HOMO}², and -OH preferentially attacked sites with higher FED_{HOMO}² + FED_{LUMO}² values [41,42]. It can be seen that N (1) and N (4) positions in the piperazine ring showed higher FED_{HOMO}² values, implying that N (1) and N (4) were likely the primary initial positions for the direct h⁺ oxidation of CIP. C (12), C (14), and C (22) exhibited a more positive point charge than others, revealing that C (12), C (14), and C (22) might be preferentially attacked by O₂^{·-} through a nucleophilic reaction. In addition, N (1) and C (15) were found to be with highest values of FED_{HOMO}² + FED_{LUMO}², implying that the addition of a hydroxyl radical could occur in quinolone and piperazine rings. The prediction of possible reactive sites based on theoretical calculations aligned well with the results of LC-MS/MS.

3.3.5. Transformation pathways

Based on the identification of products and prediction of reactive sites, potential photocatalytic CIP degradation pathways by ompg-C₃N₄ photocatalysts under simulated sunlight irradiation were proposed, as illustrated in Fig. 5. In summary, four major pathways were involved in the degradation of CIP, including the cleavage of the piperazine ring, defluorination, hydroxylation, as well as the ring opening and decarboxylation of quinolone.

The reactive site prediction showed that the N (1) and N (4) atoms within the piperazine ring could be easily attacked by h⁺. Therefore, pathway I was initiated by the cleavage of the piperazine ring. The N1 and N4 sites were attacked by h⁺, leading to the cleavage of the piperazine ring, thereby giving rise to *m/z* 306. On the other hand, electron transfer by O₂^{·-} could occur at the N1 and N4 sites, resulting in the formation of ammonium anion radicals. Subsequently, this radical could undergo deprotonation to generate a carbon-centered radical, which was subject to further oxidized by O₂^{·-} or ¹O₂, leading to the formation of *m/z* 362 with two keto-groups on the piperazine ring.

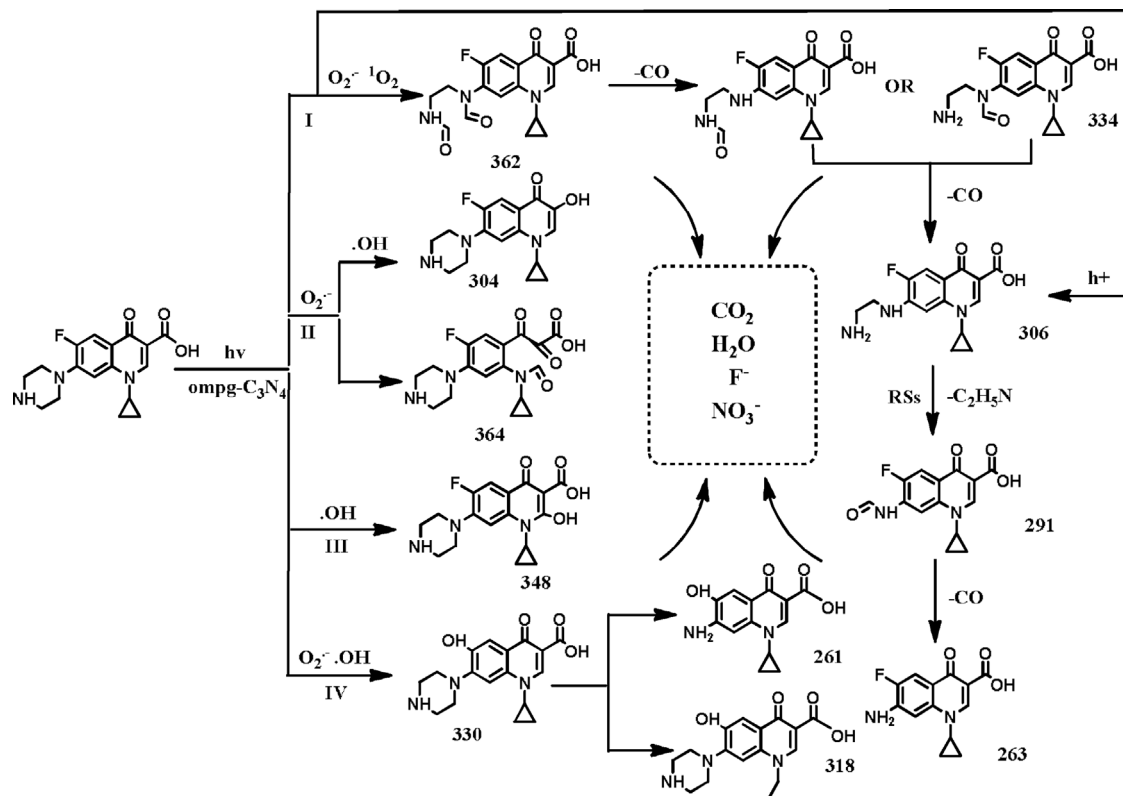
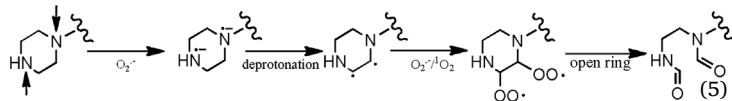


Fig. 5. Possible transformation pathways of CIP in ompg-C₃N₄ aqueous solution under simulated sunlight irradiation.

The loss of the CO group from m/z 362 produced m/z 334 and m/z 306. The formation of m/z 291 appeared to take place as a result of the loss of the C_2H_5N group of m/z 306 followed by the oxidation of RSs. As m/z 291 was formed, m/z 263 appeared via the loss of the CO group.

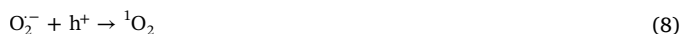


FEDs results proposed that C (14) in the quinolone groups was the most likely reaction site for $O_2\cdot^-$ attack due to its high positive charge. Consequently, pathway II might be initiated via an $O_2\cdot^-$ attack on quinolone group through the 1, 2-nucleophilic addition reaction, resulting in a peroxide. A subsequent reaction led to the cleavage of the benzene ring, which generated the ketone product m/z 364. In addition, decarboxylation could also take place at the quinolone groups of CIP, as evidenced by the formation of m/z 304. Notably, decarboxylation products were also reported in previous studies [5,43].

In terms of pathway III, the electrophilic adduct reaction with $\cdot OH$ occurred in C (15), resulting in the formation of a mono-hydroxylation product, which was similar to a structure observed in previous literature [43]. Pathway (IV) was initiated by an $O_2\cdot^-$ attack on the C(12), which subsequently underwent a $\cdot OH$ substitution, leading to the formation of the m/z 330 defluorination product. Consequently, the cleavage of the piperazine ring led to the generation of m/z 261. Moreover, m/z 330 underwent the oxidative cleavage of the cyclopropane to form m/z 318. In fact, the defluorination pathway of CIP has also been reported previously in advanced oxidation processes [2]. Further, the CIP and its byproducts could be completely mineralized to elemental molecular structures, such as NO_3^- , F^- , CO_2 , and H_2O following a prolonged irradiation time.

3.3.6. Photocatalytic mechanism

Potential photocatalytic mechanisms for the degradation of CIP were proposed based on the above results and the scientific literatures [44–46]. As illustrated in Eqs. (6)–(11), under solar light irradiation, $ompC_3N_4$ was excited by absorbing light with a wavelength < 465 nm to form electron-hole pairs. Owing to the confined space effect, electrons may rapidly migrate from the interior to the surface of the $ompC_3N_4$ through confined pore channels, leading to the high separation of CB electrons and VB h^+ [47]. As the CB potential of $ompC_3N_4$ (2.79 eV, calculated in Text S5 and Table S5) was negative enough compared to the standard reduction potential of $O_2\cdot/O_2^-$ (-0.33 eV) [29,48,49], CB electrons could be trapped by molecular oxygen in solution to form $O_2\cdot^-$. Subsequently, $O_2\cdot^-$ can react with water to form $\cdot OH$ [50]. The results of radical trapping experiment (Table 1) showed that $\cdot OH$ played negligible roles in the photocatalytic process, implying that degradation of CIP in valence band may be mainly attributed to the direct reaction with $O_2\cdot^-$ rather than $\cdot OH$. Further, 1O_2 could be generated by the reaction of $O_2\cdot^-$ with h^+ . [51] Simultaneously, the CIP molecule was easily absorbed to the surface of the $ompC_3N_4$ due to its high surface area and the $\pi-\pi$ interactions between the catalyst and substrate. Finally, RSs ($O_2\cdot^-$, h^+ , 1O_2 , $\cdot OH$) on the $ompC_3N_4$ surface reacted with CIP molecule, resulting in the decomposition and eventual complete mineralization of CIP.



3.4. Comparison with other fluoroquinolones

In order to investigate the effects of structural differences on the degradation of FQs, the degradation of CIP was compared to other fluoroquinolones, including enrofloxacin (ENR), norfloxacin (NOR), ofloxacin (OFL), lomefloxacin (LOM), fleroxacin (FLE), and flumequine (FLU). As shown in Fig. 6, a noteworthy difference in reaction rates was observed among the FQs, which were found to follow the order ENR > CIP ~ OFL ~ FLE > LOM > NOR > FLU. Without a piperazine ring, FLU exhibited significantly lower reactivity than other FQs, indicating that the piperazine moiety was the primary reactive moiety for RSs attack during the photocatalytic process of $ompC_3N_4$. This result aligned well with reactive site identification results and previous research [36]. In addition, FQs with the cyclopropane ring (i.e., CIP and ENR) demonstrated higher degradation efficiencies than those without the cyclopropane ring (NOR, LOM). We noted that the FQs, which contained tertiary N (4) amine (ENR, OFL, FLP) were found to have much higher activity than those with a secondary amine (CIP, LOM, NOR). This finding strongly verified that the tertiary N (4) amine in the piperazine ring was the primary reactive site for RSs attack during the $ompC_3N_4$ photocatalytic process. In addition, LOM which contained a methyl in the piperazine moiety and a fluorine in its quinolone moiety, exhibited higher reactivity than NOR toward $ompC_3N_4$ photocatalysis. The higher reactivity of LOM might be explained by the electron-donating effect of methyl on the piperazine moiety. Another reason was that the fluorine atom attached to the benzene ring of the LOM may potentially be substituted by a hydroxyl group [52].

3.5. Antibacterial activity

An antibacterial activity assay was performed using *E. coli* as the reference organism [43,53]. Fig. 7 presents the variations in the inhibition zone of CIP solutions during the photocatalytic process. The inhibition zone of the initial CIP solution was determined to be 19.7 cm, indicating that the CIP solution exhibited antibacterial activity. As the degradation proceeded, the inhibition zone of the treated solutions gradually decreased, and finally disappeared with an increasing

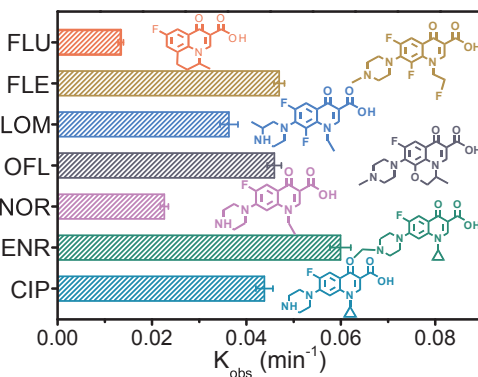


Fig. 6. $ompC_3N_4$ photocatalytic degradation kinetic rate constant of fluoroquinolones under simulated sunlight irradiation.

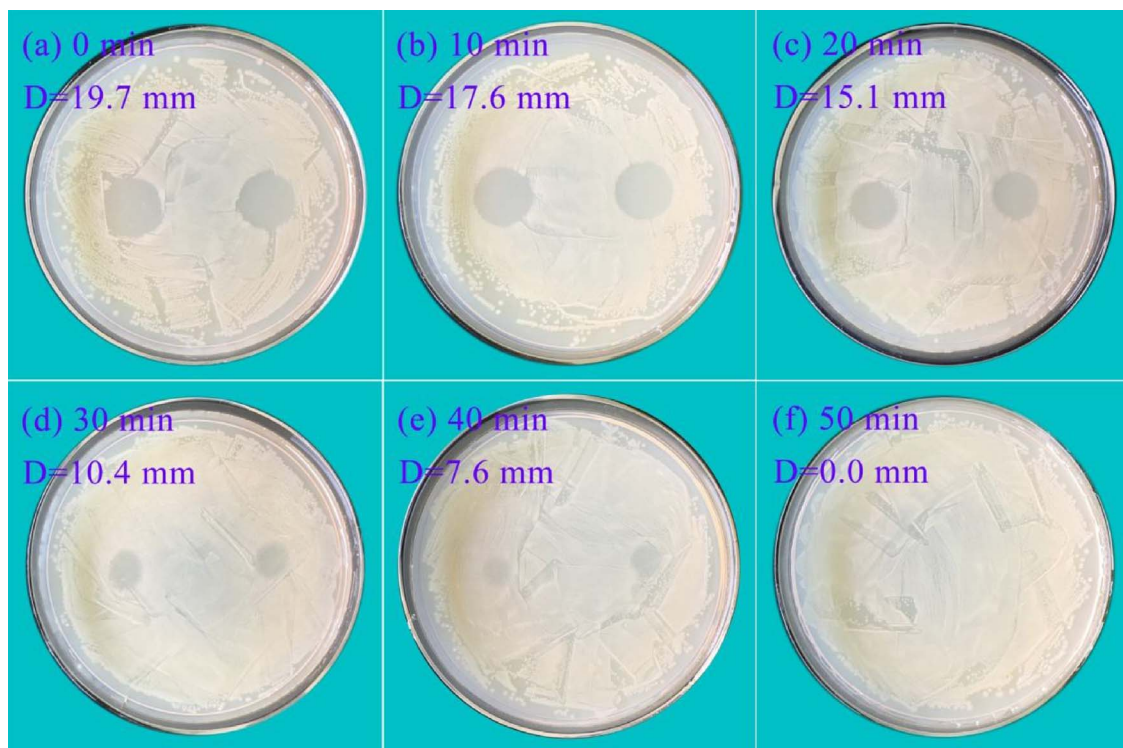


Fig. 7. *Escherichia coli* inhibition halo at different times of ompg-C₃N₄ photocatalytic reaction.

irradiation time of up to 50 min. This result implied a significant decline in the residual antibacterial activity of treated solutions during the ompg-C₃N₄ photocatalytic process. Previous studies have indicated that the fragmentation of quinolone moieties and its peripheral moieties (e.g., piperazine ring, carboxyl, and F) may lead to the deactivation of ciprofloxacin [4,43]. In the current work, LC-MS/MS and IC results revealed that the photocatalytic degradation of CIP underwent the cleavage of the piperazine ring defluorination, as well as the ring opening and decarboxylation of quinolone, which can weaken the antibacterial activity of CIP. Therefore, it can be concluded that ompg-C₃N₄ provided a very desirable performance in antibacterial activity reduction and mineralization of CIP, which is anticipated to have utility in potable water and wastewater treatment applications under simulated sunlight irradiation.

3.6. Effects of water constituents and matrices on the degradation of CIP

As shown in Fig. 8(a), no apparent effects on CIP removal were found in the presence of Na⁺, SO₄²⁻, and Cl⁻. In contrast, divalent metal cations (Ca²⁺, Mg²⁺, and Cu²⁺), particularly the transition metal Cu²⁺, significantly decreased the removal efficiency of CIP. This detrimental effect may be attributed to the scavenging of the conduction band electrons that are required for the formation of O₂^{·-} by

metal ions [54]. In addition, the presence of HA and HCO₃⁻ inhibited the photocatalytic degradation of CIP. This inhibition may be ascribed to the competition for RSs by HA and HCO₃⁻ [55]. In addition, HA can absorb sunlight and weaken the radiant flux that is necessary for ompg-C₃N₄ [56].

In order to assess the feasibility of applying the sunlight-driven ompg-C₃N₄ photocatalytic process to degrade antibiotics under ambient conditions, the degradation of CIP was carried out in various water matrices (DI water, Pearl River water, WWTP water, South China Sea water). As shown in Fig. 8(b), compared to DI water, the degradation of CIP was slightly inhibited in all natural waters. The reduced degradation efficiency of CIP in natural water matrices might be attributed to the combined effects of coexisting constituents (Table S1), which were discussed in the previous section. The high TOC and UV₄₀₀ absorbance value in Pearl River water and WWTP water may be the main reason to account for their low degradation efficiencies. In contrast, the detrimental effect of South China Sea water can be explained by the presence of high concentrations of cations (e.g., Mg²⁺, Ca²⁺, and Cu²⁺). Therefore, it can be concluded that the sunlight-driven ompg-C₃N₄ photocatalytic process may also be effectively applied for the remediation of CIP in river water, seawater, as well as WWTP effluent water.

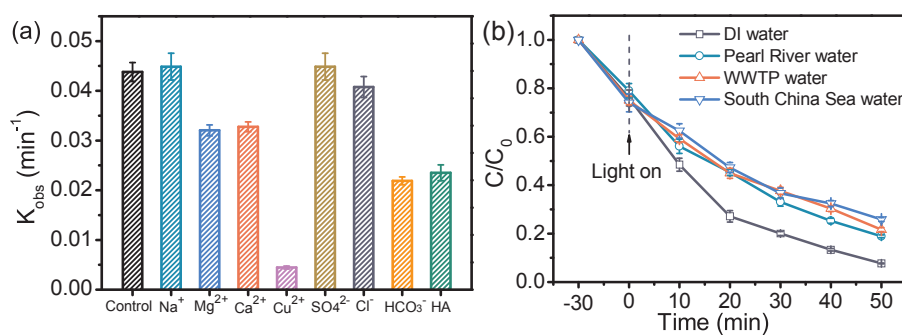


Fig. 8. (a) Effect of ions and humic acid (HA) on the photocatalytic degradation of CIP in DI water. (b) Degradation of CIP by the ompg-C₃N₄ photocatalytic oxidation in different water matrices.

4. Conclusion

In conclusion, a sunlight-driven photocatalyst ompg-C₃N₄ was prepared by using SBA-15 as the template. In comparison to bulk g-C₃N₄, ompg-C₃N₄ exhibited enhanced photocatalytic activity in the degradation of CIP. This augmented photocatalytic performance might be attributed to the large specific surface area and effective charge separation of ompg-C₃N₄. The disappearance of CIP followed the Langmuir–Hinshelwood (L–H) kinetic model, and the degradation of CIP occurred primarily on the surface of ompg-C₃N₄. ESR technology and radical scavenger experiments confirmed that O₂^{·-} and h⁺ played significant roles during the photocatalytic degradation of CIP. Based on the identification of intermediates using HPLC-MS/MS, and the prediction of reactive sites via the comparison of both similar structures and FEDs, the photocatalytic degradation pathways of CIP were proposed. A comparison of the degradation of fluoroquinolones (FQs) revealed that the piperazine moiety played a significant effect in the degradation of FQs during the ompg-C₃N₄ photocatalytic process. A residual antibiotic activity experiment revealed that the antibiotic activity of a CIP solution could be effectively reduced by ompg-C₃N₄ under simulated sunlight irradiation. The photocatalytic degradation of CIP in natural water matrix revealed that the sunlight-driven ompg-C₃N₄ photocatalytic process could be efficiently applied for the remediation of CIP in river water, seawater, as well as WWTP effluent water. Hence, the present study suggested that the ompg-C₃N₄ simulated sunlight photocatalysis process is a promising treatment technology for the elimination of the antibiotic activity and mineralization of FQs under ambient conditions.

Acknowledgements

This work was supported by the National Natural Science Foundation of China (No. 21677040 and 21377031), the Innovative Team Program of High Education of Guangdong Province (2015KCXTD007).

Appendix A. Supplementary data

Supplementary data associated with this article can be found, in the online version, at <https://doi.org/10.1016/j.apcatb.2018.01.024>.

References

- [1] R. Hirsch, T. Ternes, K. Haberer, K.L. Kratz, *Sci. Total Environ.* 225 (1999) 109–118.
- [2] Y. Ji, C. Ferronato, A. Salvador, X. Yang, J.M. Chovelon, *Sci. Total Environ.* 472C (2013) 800–808.
- [3] J.S. Wolfson, D.C. Hooper, *Clin. Microbiol. Rev.* 2 (1989) 378–424.
- [4] T. Paul, M.C. Dodd, T.J. Strathmann, *Water Res.* 44 (2010) 3121–3132.
- [5] C. Jiang, Y. Ji, Y. Shi, J. Chen, T. Cai, *Water Res.* 106 (2016) 507–517.
- [6] E.M. Golet, I. Xifra, H. Siegrist, A.C. Alder, W. Giger, *Environ. Sci. Technol.* 37 (2003) 3243–3249.
- [7] A.J. Watkinson, E.J. Murby, S.D. Costanzo, *Water Res.* 41 (2007) 4164–4176.
- [8] K. Deyong, L. Bin, Y. Hui, C. Haoyi, M. Jincai, C. Minhua, W. Aijie, R. Nanqi, *Water Res.* 72 (2015) 281–292.
- [9] C. Liu, V. Nanaboina, G.V. Korshin, W. Jiang, *Water Res.* 46 (2012) 5235–5246.
- [10] D.A.M. Alexandrino, A.P. Mucha, C.M.R. Almeida, W. Gao, Z. Jia, M.F. Carvalho, *Sci. Total Environ.* 581–582 (2017) 359–368.
- [11] N. Barhoumi, L. Labiad, M.A. Oturan, N. Oturan, A. Gadri, S. Ammar, E. Brillas, *Chemosphere* 141 (2015) 250–257.
- [12] M. Sayed, M. Ismail, S. Khan, S. Tabassum, H.M. Khan, *Environ. Technol.* 37 (2015) 590–602.
- [13] P. Chen, F. Wang, Z.F. Chen, Q. Zhang, Y. Su, L. Shen, K. Yao, Y. Liu, Z. Cai, W. Lv, *Appl. Catal. B Environ.* 204 (2017) 250–259.
- [14] J.C. Duran-Alvares, E. Avella, R. Maria Ramirez-Zamora, R. Zanella, *Catal. Today* 266 (2016) 175–187.
- [15] X. Cai, J. He, L. Chen, K. Chen, Y. Li, K. Zhang, Z. Jin, J. Liu, C. Wang, X. Wang, *Chemosphere* 171 (2017) 192–201.
- [16] Q. Han, B. Wang, Y. Zhao, C. Hu, L. Qu, *Angew. Chem. Int. Ed.* 54 (2015) 11433–11437.
- [17] W. Yu, D. Xu, T. Peng, J. Mater. Chem. A 3 (2015) 19936–19947.
- [18] X. Wang, S. Blechert, M. Antonietti, *ACS Catal.* 2 (2012) 1596–1606.
- [19] C. Chang, Y. Fu, M. Hu, C. Wang, G. Shan, L. Zhu, *Appl. Catal. B Environ.* 142 (2013) 553–560.
- [20] Z. Huang, F. Li, B. Chen, T. Lu, Y. Yuan, G. Yuan, *Appl. Catal. B Environ.* 136 (2013) 269–277.
- [21] F. Wang, P. Chen, Y. Feng, Z. Xie, Y. Liu, Y. Su, Q. Zhang, Y. Wang, K. Yao, W. Lv, *Appl. Catal. B Environ.* 207 (2017) 103–113.
- [22] P. Chen, F. Wang, Q. Zhang, Y. Su, L. Shen, K. Yao, Z.-F. Chen, Y. Liu, Z. Cai, W. Lv, G. Liu, *Chemosphere* 172 (2017) 193–200.
- [23] X. Gao, X. Jiao, L. Zhang, W. Zhu, X. Xu, T. Chen, H. Ma, *RSC Adv.* 5 (2015) 76963–76972.
- [24] D.B. Hernandez-Uresti, A. Vazquez, D. Sanchez-Martinez, S. Obregon, *J. Photochem. Photobiol. A Chem.* 324 (2016) 47–52.
- [25] H. Xu, H. Zhao, Y. Song, W. Yan, Y. Xu, H. Li, L. Huang, S. Yin, Y. Li, Q. Zhang, H. Li, *Mater. Sci. Semicond. Process.* 39 (2015) 726–734.
- [26] J. Xue, S. Ma, Y. Zhou, Q. Wang, *RSC Adv.* 5 (2015) 88249–88257.
- [27] M. Yan, F.F. Zhu, W. Gu, L. Sun, W.D. Shi, Y.Q. Hua, *RSC Adv.* 6 (2016) 61162–61174.
- [28] H. Xiao, J. Zhu, A. Thomas, *RSC Adv.* 5 (2015) 105731–105734.
- [29] G.Y. Li, X. Nie, J.Y. Chen, Q. Jiang, T.C. An, P.K. Wong, H.M. Zhang, H.J. Zhao, H. Yamashita, *Water Res.* 86 (2015) 17–24.
- [30] T. Fotiou, T.M. Triantis, T. Kaloudis, K.E. O’Shea, D.D. Dionysiou, A. Hiskia, *Water Res.* 90 (2016) 52–61.
- [31] T. An, H. Yang, G. Li, W. Song, W.J. Cooper, X. Nie, *Appl. Catal. B Environ.* 94 (2010) 288–294.
- [32] T. An, J. An, Y. Gao, G. Li, H. Fang, W. Song, *Appl. Catal. B Environ.* 164 (2015) 279–287.
- [33] S. Ahmed, M.G. Rasul, R. Brown, M.A. Hashib, *J. Environ. Manag.* 92 (2011) 311–330.
- [34] X. Lei, G. Wang, F. Ma, Y. Zhao, L. Nan, Y. Guo, Y. Xia, *Appl. Surf. Sci.* 258 (2012) 7039–7046.
- [35] Junfeng Yang, Wenlong Lifeng, Yueping Wang, Chen Jing, Duan Yanpei, *J. Environ. Sci.* 23 (2011) 7151–7154.
- [36] A.S. Giri, A.K. Golder, *RSC Adv.* 4 (2014) 6738–6745.
- [37] M. Chen, W. Chu, J. Hazard. Mater. 219 (2012) 183–189.
- [38] S. Ding, J. Niu, Y. Bao, L. Hu, J. Hazard. Mater. 262 (2013) 812–818.
- [39] Y. Ji, Y. Fan, K. Liu, D. Kong, J. Lu, *Water Res.* 87 (2015) 1–9.
- [40] M. Sayed, M. Ismail, S. Khan, S. Tabassum, H.M. Khan, *Environ. Technol.* 37 (2016) 590–602.
- [41] Y. Ji, L. Zhou, C. Ferronato, X. Yang, A. Salvador, C. Zeng, J.M. Chovelon, *J. Photochem. Photobiol. A Chem.* 254 (2013) 35–44.
- [42] H.S. Wahab, T. Bredow, S.M. Aliwi, *Surf. Sci.* 603 (2009) 664–669.
- [43] H.S. Ou, J.S. Ye, S. Ma, C.H. Wei, N.Y. Gao, J.Z. He, *Chem. Eng. J.* 289 (2016) 391–401.
- [44] Z. Hui, L. Zhao, F. Geng, L.H. Guo, B. Wan, Y. Yu, *Appl. Catal. B Environ.* 180 (2016) 656–662.
- [45] J. Xia, J. Di, H. Li, X. Hui, H. Li, S. Guo, *Appl. Catal. B Environ.* 181 (2016) 260–269.
- [46] J. Chen, H. Che, K. Huang, C. Liu, W. Shi, *Appl. Catal. B Environ.* 192 (2016) 134–144.
- [47] J. Liu, J. Yan, H. Ji, Y. Xu, L. Huang, Y. Li, Y. Song, Q. Zhang, H. Xu, H. Li, *Mater. Sci. Semicond. Process.* 46 (2016) 59–68.
- [48] J. Ma, C. Wang, H. Hong, *Appl. Catal. B Environ.* 184 (2016) 28–34.
- [49] X. Lin, B. Wei, X. Zhang, M. Song, S. Yu, Z. Gao, H. Zhai, L. Zhao, G. Che, *Sep. Purif. Technol.* 169 (2016) 9–16.
- [50] F. Wang, P. Chen, Y. Feng, Z. Xie, Y. Liu, Y. Su, Q. Zhang, Y. Wang, K. Yao, W. Lv, G. Liu, *Appl. Catal. B Environ.* 207 (2017) 103–113.
- [51] F. Wang, Y. Wang, Y. Feng, Y. Zeng, Z. Xie, Q. Zhang, Y. Su, P. Chen, Y. Liu, K. Yao, W. Lv, G. Liu, *Appl. Catal. B Environ.* 221 (2018) 510–520.
- [52] W. Song, W.J. Cooper, B.M. Peake, S.P. Mezyk, M.G. Nickelsen, K.E. O’Shea, *J. Phys. Chem. A* 113 (2009) 7846–7851.
- [53] J.-s. Ye, J. Liu, H.-s. Ou, L.-l. Wang, *Chemosphere* 165 (2016) 311–319.
- [54] T.A. And, G. Madras, *Ind. Eng. Chem. Res.* 46 (2007) 1–7.
- [55] Y. Ji, Z. Lei, C. Ferronato, A. Salvador, Y. Xi, J.M. Chovelon, *Appl. Catal. B Environ.* 140–141 (2013) 457–467.
- [56] L. Zhou, Y. Ji, C. Zeng, Y. Zhang, Z. Wang, X. Yang, *Water Res.* 47 (2013) 153–162.

Update

Applied Catalysis B: Environmental

Volume 238, Issue , 15 December 2018, Page 673

DOI: <https://doi.org/10.1016/j.apcatb.2018.03.097>



Corrigendum

Corrigendum to “Photocatalytic degradation of fluoroquinolone antibiotics using ordered mesoporous g-C₃N₄ under simulated sunlight irradiation: Kinetics, mechanism, and antibacterial activity elimination” [Appl. Catal. B: Environ. 227 (2018) 114–122]



Fengliang Wang^a, Yiping Feng^a, Ping Chen^b, Yingfei Wang^a, Yuehan Su^a, Qianxin Zhang^a, Yongqin Zeng^a, Zhijie Xie^a, Haijin Liu^c, Yang Liu^d, Wenying Lv^a, Guoguang Liu^{a,*}

^a Institute of Environmental Health and Pollution Control, School of Environmental Science and Engineering, Guangdong University of Technology, Guangzhou, Guangdong 510006, China

^b School of Environment, Tsinghua University, Beijing 100084, China

^c School of Environment, Henan Normal University, Key Laboratory for Yellow River and Huaihe River Water Environment and Pollution Control, Xinxiang, 453007, China

^d Guangdong University of Petrochemical Technology, Maoming, 525000, China

The authors regret to inform that there were some mistakes in Fig. 4 (b).

The authors would like to apologise for any inconvenience caused.

Fig. 4 (b) should be corrected to

